

Ab initio Real-Time Quantum Dynamics of Charge Carriers in Momentum Space

Zhenfa Zheng¹, Yongliang Shi^{1,2,3*}, Jin-jian Zhou⁴, Oleg V. Prezhdo⁵, Qijing Zheng^{1*} and Jin Zhao^{1,6*}

^{1*} Department of Physics, ICQD/Hefei National Research Center for Physical Sciences at Microscale, University of Science and Technology of China, Hefei, 230026, Anhui, China .

^{2*} Center for Spintronics and Quantum Systems, State Key Laboratory for Mechanical Behavior of Materials, School of Materials Science and Engineering, Xi'an Jiaotong University, Xi'an, 710049, Shanxi, China .

^{3*} China 2 State Key Laboratory of Surface Physics and Department of Physics, Fudan University, Shanghai, 200433, China .

⁴ School of Physics, Beijing Institute of Technology, Beijing, 100081, China .

⁵ Departments of Chemistry, Physics, and Astronomy, University of Southern California, Los Angeles, 90089, California, USA .

^{6*} Department of Physics and Astronomy, University of Pittsburgh, Pittsburgh, 15260, Pennsylvania, USA .

*Corresponding author(s). E-mail(s): sylcliff@xjtu.edu.cn; zqj@ustc.edu.cn; zhaojin@ustc.edu.cn;

Abstract

Application of the nonadiabatic molecular dynamics (NAMD) approach is severely limited to studying carrier dynamics in the momentum space, since a supercell is required to sample the phonon excitation and electron-phonon (*e-ph*) interaction at different momenta in a molecular dynamics simulation. Here, we develop an *ab initio* approach for the real-time quantum dynamics for charge carriers in the momentum space (NAMD-**k**) by directly introducing the *e-ph* coupling into the Hamiltonian based on the harmonic approximation. The NAMD-**k**

approach maintains the quantum zero-point energy and proper phonon dispersion, and includes memory effects of phonon excitation. The application of NAMD_**k** to the hot carrier dynamics in graphene reveals the phonon-specific relaxation mechanism. An energy threshold of 0.2 eV, defined by two optical phonon modes strongly coupled to the electrons, separates the hot electron relaxation into fast and slow regions with the lifetimes of pico- and nano-seconds, respectively. The NAMD_**k** approach provides a powerful tool to understand real-time carrier dynamics in the momentum space for different materials.

1 Introduction

Tracking the quantum dynamics of excited charge carriers in solid materials in multi-dimensions including time and energy domains, as well as real and momentum spaces is fundamental to the understanding of many dynamical processes in optoelectronics, spin- and valley-tronics, solar energy conversion, and so on.[1–6] Different time-resolved experimental techniques, including ultrafast time- and angle-resolved photoemission spectroscopy (TR-ARPES) with time, energy, and momentum resolution, have been rapidly developed and applied to investigate charge carrier dynamics in various materials.[7–9] However, without the input of *ab initio* investigations, it is rather difficult to understand the physical mechanisms behind the experimental spectra. Thus, it is urgent to develop an *ab initio* simulation approach to achieve a state-of-the-art understanding of multi-dimensional carrier dynamics in solids.

Ab initio approach based on perturbation theory provides useful information to understand carrier lifetimes governed by different scattering mechanisms. However, the real-time dynamics information cannot be obtained straightforwardly. In recent decades, the real-time time-dependent density functional theory (TDDFT) based on Ehrenfest dynamics[10–14] and nonadiabatic molecular dynamics (NAMD) approaches combining time-dependent Kohn-Sham (TDKS) theory and surface hopping have been applied to investigate the quantum dynamics of excited charge carriers.[6, 15–18] The electron-phonon (*e-ph*) coupling, spin-orbit coupling (SOC), and many-body electron-hole interaction have been included with different theoretical strategies.[19–24] However, in all these methods, it is rather difficult to achieve real-time carrier dynamics in the momentum space. In previous NAMD simulations, the phonon excitation is described using *ab initio* molecular dynamics (AIMD) within periodic boundary conditions, and only phonons at the Γ point are included. Thus, the electron transition from one **k** to another through *e-ph* is forbidden even though the electronic states can be simulated using multi-**k** grids. To sample the phonon excitation and electron-phonon interaction at different momenta, a supercell needs to be used, so that phonons at other **q**-points can be folded to the Γ point. The **q**-grid density is determined by the size of the supercell, and due to the computational cost, usually, only a few **q**-points can

be included in the NAMD simulation.[6, 19, 21, 25, 26] As a contrast, the *e-ph* scattering between different momenta often needs to be simulated with a very dense of \mathbf{k} - and \mathbf{q} -grids, especially when the electronic band dispersion is strong. Therefore, an *ab initio* approach to describe the real-time quantum dynamics of photoexcited carriers in the momentum space is essential.

In this work, by introducing the *e-ph* coupling elements into the time-propagation Hamiltonian, we have extended the *ab initio* NAMD approach from the real-space (labeled as NAMD_ \mathbf{r}) to the momentum space (NAMD_ \mathbf{k}). Different from the previous NAMD_ \mathbf{r} approach, where an AIMD simulation using a large supercell is required for \mathbf{q} -grid sampling, in NAMD_ \mathbf{k} the \mathbf{k} and \mathbf{q} sampling is performed by the calculation of *e-ph* matrix elements using a unit cell. The computational cost is significantly reduced. Moreover, the NAMD_ \mathbf{k} approach provides a straightforward picture not only for the dynamics of excited electrons in the momentum space, but also the time-dependent phonon excitation of the lattice due to the *e-ph* scattering. The phonon zero-point energy as well as the phonon dispersion are accurately represented with memory effects. Using this approach, we have investigated the hot carrier dynamics in graphene. It is found that there is an energy threshold at 0.2 eV above the Fermi level (E_f). The threshold separates the hierarchical relaxation dynamics from fast [picosecond(ps)] to slow [nanosecond(ns)] regions. The intervalley *e-ph* scattering is activated in the fast region but strongly suppressed in the slow region. The energy threshold is determined by strongly coupled optical phonon modes A_1 and E_{2g} . Our work not only reveals the phonon mode-specific energy threshold for hot electron relaxation in graphene, but also provides a powerful tool which can be widely applied to study excited carrier dynamics in different solid state systems with momentum space resolution.

2 Methodology

In the NAMD_ \mathbf{r} approach, the charge carrier (electron or hole) wavefunction is expanded in the basis of instantaneous adiabatic Kohn-Sham (KS) orbitals, which are obtained by solving the KS equation at atomic configuration $\mathbf{R}(t)$,

$$|\Psi(\mathbf{r}; \mathbf{R}(t))\rangle = \sum_n c_n(t) |\psi_n(\mathbf{r}; \mathbf{R}(t))\rangle. \quad (1)$$

Based on the classical-path approximation (CPA), $\mathbf{R}(t)$ can be obtained by AIMD. The charge carrier wavefunction follows the time-dependent Schrödinger equation (TDSE)

$$i\hbar \frac{\partial}{\partial t} |\Psi(\mathbf{r}; \mathbf{R}(t))\rangle = \hat{H}^{el}(\mathbf{r}; \mathbf{R}(t)) |\Psi(\mathbf{r}; \mathbf{R}(t))\rangle. \quad (2)$$

Then, a set of differential equations for the coefficients $c_m(t)$ is produced

$$i\hbar\dot{c}_m(t) = \sum_n c_n(t)[\epsilon_n - i\hbar d_{mn}], \quad (3)$$

where ϵ_n is the energy of the adiabatic KS state, and d_{mn} is the NAC between KS states m and n . The NAC can be written as

$$d_{mn} = \langle \psi_m | \frac{d}{dt} | \psi_n \rangle = \frac{\langle \psi_m | \Delta_{\mathbf{R}} \hat{H}^{el} | \psi_n \rangle}{\epsilon_n - \epsilon_m} \cdot \dot{\mathbf{R}}. \quad (4)$$

Here, ϵ_m and ϵ_n are the eigenvalues of the KS orbitals m and n , d_{mn} is the *e-ph* coupling term, and $\dot{\mathbf{R}}$ is the nuclear velocity. NAC is the crucial term in the NAMD_r simulation. It determines not only the time-dependent coefficient evolution, but also the hopping probability in the subsequent surface hopping step.[15, 16] According to Bloch's theory, if ψ_m and ψ_n have different \mathbf{k} vectors, the NAC is zero (see more details in the Supplementary Materials). The essential reason is that in the AIMD simulation with periodic conditions, only phonon modes at the Γ point are included. Therefore, the NAMD_r approach can not efficiently simulate the carrier dynamics in the momentum space.

The NAMD_k approach is based on the harmonic approximation. Here, different with eq. (1), we expand the charge carrier wavefunction using the KS orbitals of the equilibrium atomic configuration \mathbf{R}_0

$$|\Psi(\mathbf{r}; \mathbf{R}(t))\rangle = \sum_{n\mathbf{k}} c_{n\mathbf{k}}(t) |\psi_{n\mathbf{k}}(\mathbf{r}; \mathbf{R}_0)\rangle, \quad (5)$$

where the KS orbital $|\psi_{n\mathbf{k}}(\mathbf{r}; \mathbf{R}_0)\rangle$ with band index n and momentum \mathbf{k} is the eigenstate of the equilibrium configuration \mathbf{R}_0 . Naturally, the charge carrier Hamiltonian is divided into two parts

$$\hat{H}^{el}(\mathbf{r}; \mathbf{R}(t)) = \hat{H}^0(\mathbf{r}; \mathbf{R}_0) + \Delta V(\mathbf{r}; \mathbf{R}(t)), \quad (6)$$

where ΔV is the variation of the potential induced by nuclear displacements $\Delta\mathbf{R}(t) = \mathbf{R}(t) - \mathbf{R}_0$. Combining the above equations, we get a new coefficient evolution equation

$$i\hbar\frac{d}{dt}c_{m\mathbf{k}'}(t) = \sum_{n\mathbf{k}} (H_{m\mathbf{k}',n\mathbf{k}}^0 + H_{m\mathbf{k}',n\mathbf{k}}^{ep})c_{n\mathbf{k}}(t). \quad (7)$$

Here,

$$H_{m\mathbf{k}',n\mathbf{k}}^0 = \langle \psi_{m\mathbf{k}'} | \hat{H}^0 | \psi_{n\mathbf{k}} \rangle = \epsilon_{n\mathbf{k}} \delta_{mn,\mathbf{k}'\mathbf{k}}, \quad (8)$$

is the diagonal KS energy matrix and

$$H_{m\mathbf{k}',n\mathbf{k}}^{ep} = \langle \psi_{m\mathbf{k}'} | \Delta V | \psi_{n\mathbf{k}} \rangle, \quad (9)$$

is the *e-ph* coupling Hamiltonian. m and n are the notation of the KS orbitals, and \mathbf{k} and \mathbf{k}' are the notation of the momentum.

Transformed into the momentum space, the *e-ph* term can be rewritten as

$$\begin{aligned} H_{m\mathbf{k}',n\mathbf{k}}^{ep} &= \frac{1}{\sqrt{N_p}} \sum_{\mathbf{q}\nu} \langle u_{m\mathbf{k}'} | \Delta_{\mathbf{q}\nu} v(\mathbf{r}; \mathbf{R}_0) | u_{n\mathbf{k}} \rangle_{uc} \delta_{\mathbf{q},\mathbf{k}'-\mathbf{k}} Q_{\mathbf{q}\nu}(t) / l_{\mathbf{q}\nu} \\ &= \frac{1}{\sqrt{N_p}} \sum_{\nu} g_{mn\nu}(\mathbf{k}, \mathbf{q}) Q_{\mathbf{q}\nu}(t) / l_{\mathbf{q}\nu} \Big|_{\mathbf{q}=\mathbf{k}'-\mathbf{k}}, \end{aligned} \quad (10)$$

where N_p is the number of unit cells according to the Born-von Kármán boundary conditions, $Q_{\mathbf{q}\nu}(t)$ is the normal mode coordinate of the corresponding vibration mode of phonon with momentum \mathbf{q} in the branch ν , $l_{\mathbf{q}\nu}$ is the “zero-point” displacement amplitude, and $g_{mn\nu}(\mathbf{k}, \mathbf{q})$ is the *e-ph* matrix element. In this way, the NAC in the NAMD_r approach is replaced by the *e-ph* coupling Hamiltonian in eq. (10), which naturally includes the coupling between electronic states with different momenta \mathbf{k} and the scattering with phonons at different momenta \mathbf{q} .

In the NAMD_k method, to get the real-time carrier dynamics, the *e-ph* coupling matrix element $g_{mn\nu}(\mathbf{k}, \mathbf{q})$ and the time-dependent normal mode coordinate $Q_{\mathbf{q}\nu}(t)$ are required. $g_{mn\nu}(\mathbf{k}, \mathbf{q})$ can be calculated by the DFPT method using the primitive cell[27] or finite difference method with non-diagonal supercells.[28] $Q_{\mathbf{q}\nu}(t)$ can be obtained using different methods. For example, it can be expressed in terms of phonon populations as

$$Q_{\mathbf{q}\nu}(t) = l_{\mathbf{q}\nu} \sqrt{n_{\mathbf{q}\nu} + \frac{1}{2}} (e^{-i\omega_{\mathbf{q}\nu}t} + e^{i\omega_{-\mathbf{q}\nu}t}), \quad (11)$$

where the initial population of phonons at $t = 0$ (t_0) is given by the Bose-Einstein distribution $n_{\mathbf{q}\nu} = \frac{1}{e^{\hbar\omega_{\mathbf{q}\nu}/k_B T} - 1}$. It can also be obtained from the molecular dynamics simulation using the normal mode decomposition method.[29] Finally, the fewest switches surface hopping (FSSH) is applied to include the stochastic factor of the carrier dynamics. More details can be found in the Supplementary Materials.

3 Results and Discussion

To verify the validity of the NAMD_k method, we choose graphene as a prototypical system and simulate the hot electron relaxation process, which has been investigated extensively.[30–40] The band structure of graphene has six Dirac cones near the E_f at K and K' points in the first Brillouin zone (BZ), which is also known as six valleys. As discussed in the Supplementary Materials, the NAMD_k approach using the $9 \times 9 \times 1$ \mathbf{k} -grid can successfully reproduce the NAMD_r results using the $9 \times 9 \times 1$ supercell.

The hot electron relaxation may involve intervalley and intravalley *e-ph* scattering. We first study dynamics with a single electron initially excited at

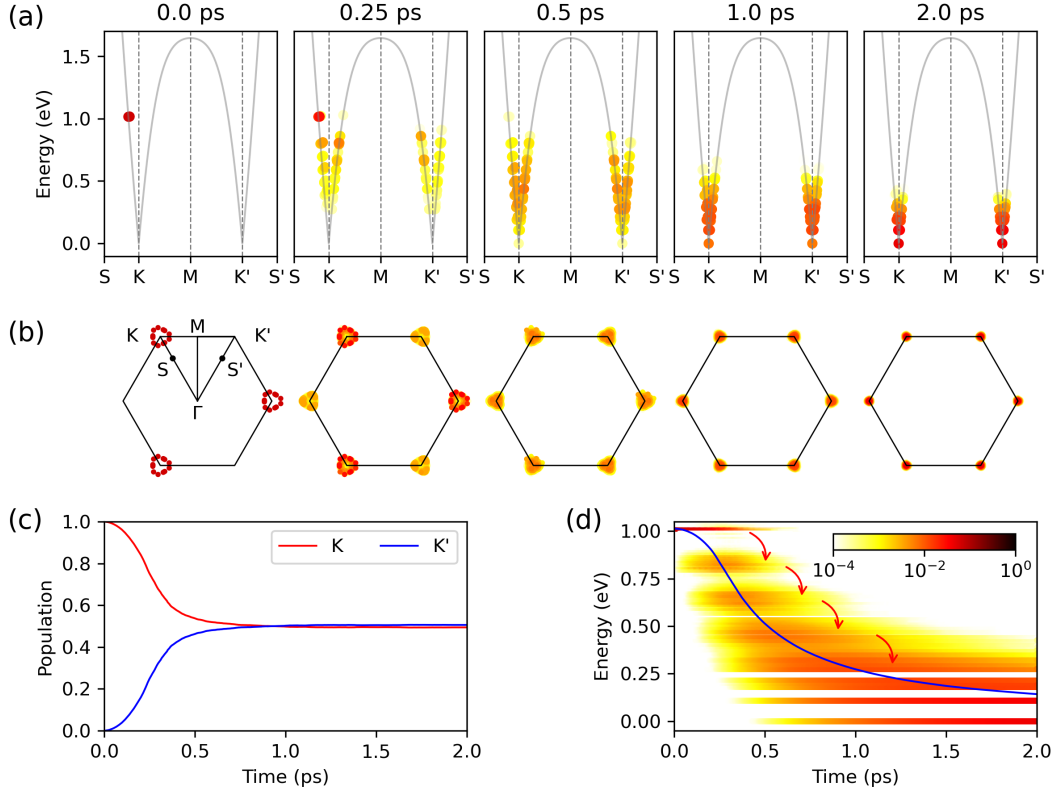


Fig. 1 Hot electron relaxation in graphene with $E_{\text{ini}} = 1.0 \text{ eV}$ using $150 \times 150 \times 1$ \mathbf{k} -grid. (a-b) Snapshots of hot electron distribution in energy and momentum space at 0, 0.25, 0.5, 1.0 and 2.0 ps. The color dots indicate the electron population in different states. (c) Time-dependent electron population in the K and K' valleys. (d) Hot electron relaxation in the energy domain. The color strips indicate the electron population in different energy states, and the blue line represents the averaged electron energy. The energy reference is E_f .

1.0 eV above the E_f ($E_{\text{ini}} = 1.0 \text{ eV}$) in the K valley. To get statistics on the quantum behavior of the excited electron, we randomly set the initially excited electron at 30 different \mathbf{k} -points in the K valley at 1.0 eV above the E_f . For each \mathbf{k} -points we sample 2×10^4 trajectories. Using $150 \times 150 \times 1$ \mathbf{k} -grid is found to be able to achieve well converged results (the \mathbf{k} -grid convergence details are presented in the Supplementary Materials). Figure 1 (a) shows five snapshots of the hot electron population in the band structure over 2 ps, and Figure 1 (b) gives the corresponding hot electron distribution in the first BZ. It can be seen that although the hot electron is initially excited in the K valley, the K - K' intervalley scattering almost immediately starts. Figure 1 (c) presents the time-dependent electron population in the K and K' valleys. The valley lifetime (τ_K), which is defined as the timescale when the equilibrium between K and K' is reached, is around 0.4 ps. The intervalley scattering suggests that the hot electron couples with phonons with large momentum. Figure 1 (d) shows the hot electron energy relaxation. The color bar indicates the electron population, and the blue line represents the averaged energy. It can be seen that there is an energy threshold for hot electron relaxation, located at around 0.2 eV above the E_f . Above the threshold energy, the relaxation is a relatively fast process,

which corresponds to energy relaxation from 1.0 eV to around 0.2 eV within 2 ps. Using a Gaussian function, the lifetime for this fast energy relaxation (τ_E) can be estimated to be 0.56 ps. Furthermore, a quantized character with an energy difference of around 0.2 eV as indicated in Figure 1 (d). Following the fast process, there happens a much slower relaxation process from 0.2 eV to the Dirac point. The timescale of the slow process is difficult to be estimated with a 2 ps simulation.

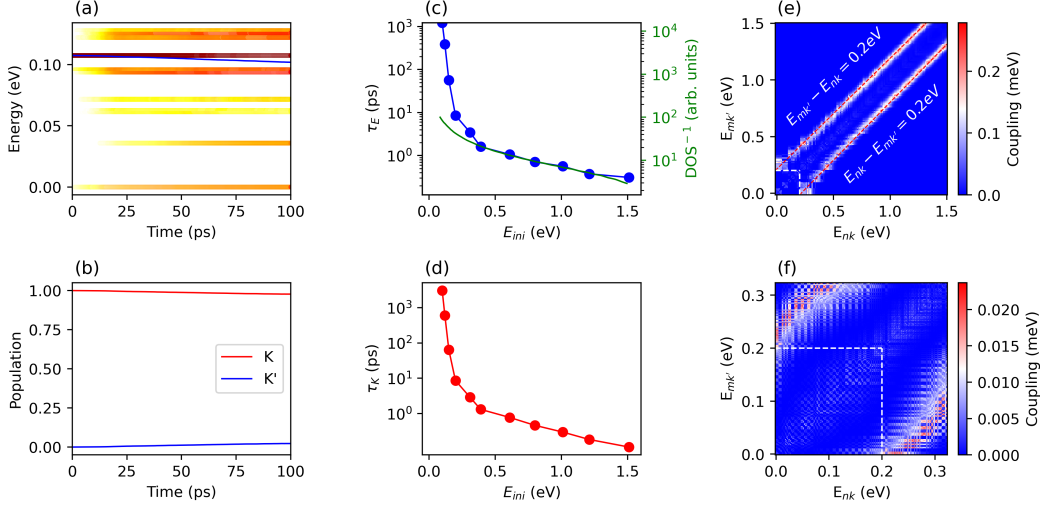


Fig. 2 Hot electron relaxation in graphene with different E_{ini} . (a) Hot electron relaxation in energy domain with $E_{ini} = 0.1$ eV. The color strips indicate the electron distribution in different energy states, and the blue line represents the averaged electron energy. The energy reference is E_f . (b) Time-dependent electron population in the K and K' valleys with $E_{ini} = 0.1$ eV. (c) The dependence of τ_E on E_{ini} . When $E_{ini} > 0.2$ eV, $150 \times 150 \times 1$ **k**-grid is used. There are fast and slow relaxation processes, and τ_E^{fast} is plotted. When $E_{ini} < 0.2$ eV, $450 \times 450 \times 1$ **k**-grid is used. There is only a slow relaxation process, and τ_E^{slow} is plotted. The green line represents the reciprocal of density of states (DOS^{-1}) at different energies. τ_E^{fast} is proportional to DOS^{-1} . The energy reference is E_f . (d) The dependence of τ_K on E_{ini} . (e-f) E -ph coupling $H_{mk',nk}^{ep} = \langle \psi_{mk'} | \Delta V | \psi_{nk} \rangle$ between states $\psi_{mk'}$ and ψ_{nk} plotted with different $E_{mk'}$ and E_{nk} scales.

To understand further the slow relaxation process close to the E_f , we perform a 100 ps NAMD_**k** simulation for hot electron relaxation with $E_{ini} = 0.1$ eV. In this case, since the density of states (DOS) become smaller when the energy is close to the E_f , a more dense of **k**-grid is required, and we use $450 \times 450 \times 1$ **k**-grid. The energy and valley dynamics are shown in Figure 2 (a-b). Both the energy and valley relaxation become much slower, and there is no longer a fast process in energy relaxation. τ_E and τ_K are estimated to be 1.2 and 3.0 ns, respectively. Such a relaxation behavior is completely different from $E_{ini} = 1.0$ eV. We further study the hot electron relaxation dynamics with different E_{ini} from 0.1 to 1.5 eV. As shown in Figure 2 (c), it is found that $E_{ini} = 0.2$ eV is a critical point for different relaxation behaviors. If $E_{ini} > 0.2$ eV, there will be both a fast and a slow relaxation process. The τ_E for the fast process (τ_E^{fast}) ranges from 0.3 to 3.0 ps, inversely proportional

to the DOS. When $E_{\text{ini}} < 0.2 \text{ eV}$, there is only the slow process and τ_E^{slow} dramatically increases by 1-3 orders of magnitude. The correlation between τ_K and E_{ini} is shown in Figure 2 (d), demonstrating a very similar trend with τ_E . When $E_{\text{ini}} > 0.2 \text{ eV}$, the equilibrium between the K and K' valleys can be reached on a ps timescale due to frequent intervalley e - ph scattering. Whereas, when $E_{\text{ini}} < 0.2 \text{ eV}$, the intervalley e - ph scattering becomes rare, and τ_K reaches a ns timescale. The slow energy relaxation process is dominated by the intravalley scattering.

In the NAMD-**r** approach, the NAC expressed in Eq. (4) is the crucial term determining the carrier dynamics. Accordingly, in the NAMD-**k** approach, the e - ph coupling $H_{m\mathbf{k}',n\mathbf{k}}^{ep} = \langle \psi_{m\mathbf{k}'} | \Delta V | \psi_{n\mathbf{k}} \rangle$ between states $\psi_{m\mathbf{k}'}$ and $\psi_{n\mathbf{k}}$ plays the key role. In Figure 2 (e-f) we plot the averaged $H_{m\mathbf{k}',n\mathbf{k}}^{ep}$, where the x and y axes represent the energy of $\psi_{m\mathbf{k}'}$ and $\psi_{n\mathbf{k}}$ (labeled as $E_{m\mathbf{k}'}$ and $E_{n\mathbf{k}}$, respectively). In Figure 2 (e), where $E_{m\mathbf{k}'}$ and $E_{n\mathbf{k}}$ range within $[0.0, 1.5] \text{ eV}$, the largest $H_{m\mathbf{k}',n\mathbf{k}}^{ep}$ can be roughly fitted by two lines, which are expressed as $|E_{m\mathbf{k}'} - E_{n\mathbf{k}}| = 0.2 \text{ eV}$, suggesting the coupling between two electronic states is the largest when the state energy difference is around 0.2 eV. Thus, when $E_{\text{ini}} > 0.2 \text{ eV}$, the hot electron prefers to relax to an electronic state 0.2 eV lower in energy, which explains the quantized character with an energy difference of 0.2 eV observed in the fast relaxation process shown in Figure 1 (d), suggesting that the hot electron relaxation is strongly coupled to phonons with energy around 0.2 eV. When $E_{\text{ini}} < 0.2 \text{ eV}$, as indicated by the square marked with the white dashed lines in Figure 2 (f), the couplings between $E_{m\mathbf{k}'}$ and $E_{n\mathbf{k}}$ are much smaller. The matrix elements close to the diagonal line, where $|E_{m\mathbf{k}'} - E_{n\mathbf{k}}|$ is very small, play a crucial role. This result implies that in this case, the coupling to the phonons with small energies is essential.

During the hot electron relaxation, the energy of the electrons transfers to the phonons through the e - ph coupling. Figure 3 shows the phonon excitation dynamics along with the hot electron relaxation. Figure 3 (a) shows the four snapshots of phonon excitation within 2 ps with $E_{\text{ini}} = 1.0 \text{ eV}$. It can be seen that within the hot electron relaxation process, only the optical modes A_1 and E_{2g} , which belong to the LO and TO branches, are notably excited. In addition, there is a minor excitation for the LA and TA modes. Figure 3 (b-c) shows the time-dependent phonon population and energies of these four different phonon modes. It can be seen that the excitations of the optical A_1 and E_{2g} modes with $\hbar\omega_{A_1} = 0.16 \text{ eV}$ and $\hbar\omega_{E_{2g}} = 0.19 \text{ eV}$ are dominant. The excitation of A_1 is responsible for the intervalley electron scattering, and both A_1 and E_{2g} contribute to the quantized character in the energy relaxation process. Together, they define the critical energy threshold around 0.2 eV. Figure 3 (d-f) presents the time-dependent phonon excitation with $E_{\text{ini}} = 0.1 \text{ eV}$. In this case, the LA and TA phonons around the Γ point excitation are dominant, as shown in Figure 3 (d) and (e). Due to the thermal energy smearing of the electronic states (see more details in the Supplementary Materials), the optical phonon mode A_1 also has a minor contribution. Since its energy is much higher than the LA and TA phonon energies, its contribution to the excited phonon energy

is still dominant. Since the energies and momenta of the LA and TA phonons are both very small, the energy and valley dynamics are much slower. The phonon excitation results explain the distinct hot electron relaxation behavior when E_{ini} is above or below the energy threshold of 0.2 eV.

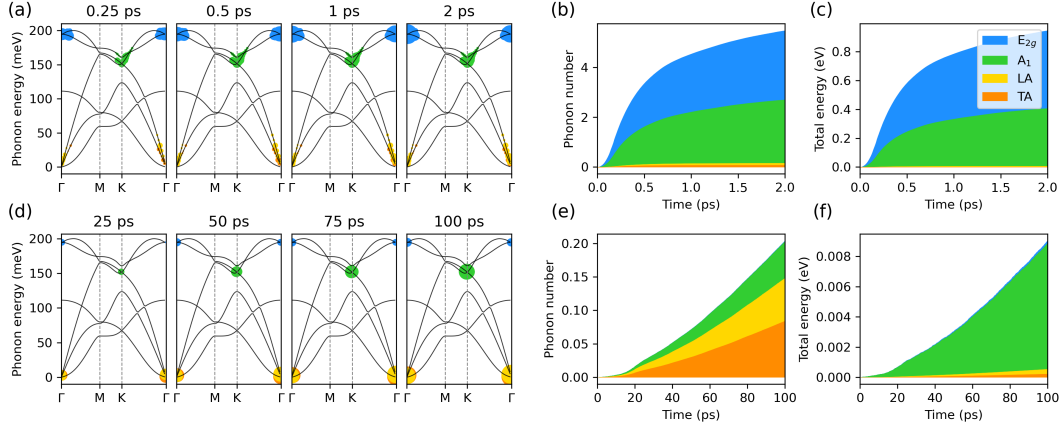


Fig. 3 Time-dependent phonon excitation during the hot electron relaxation dynamics. (a) Snapshots of phonon excitation dynamics at 0.25, 0.5, 1.0 and 2.0 ps with $E_{\text{ini}} = 1.0$ eV. Time evolution of (b) the excited phonon number and (c) the total phonon energy during the hot electron relaxation with $E_{\text{ini}} = 1.0$ eV. (d) Snapshots of the phonon excitation dynamics at 25, 50, 75 and 100 ps with $E_{\text{ini}} = 0.1$ eV. Time evolution of (e) the excited phonon number and (f) the total phonon energy during the hot electron relaxation with $E_{\text{ini}} = 0.1$ eV.

Finally, we study the multi-hot electron relaxation by simulating the electron temperature (T_e) decrease. In the TR-ARPES measurements, after photoexcitation, the hot electrons will reach equilibrium with a certain temperature through electron-electron ($e-e$) scattering, and then relax to a lower temperature through $e-ph$ coupling. Figure 4 (a) shows 5 snapshots in the T_e relaxation with initial electron temperature $T_e^{\text{ini}} = 3193$ K. In this case T_e decreases to 639 K at 10 ps. Figure 4 (b) shows the time-dependent relaxation dynamics with $T_e^{\text{ini}} = 3193, 2200$ and 1060 K. For all three cases, T_e converges to around 500 K at 10 ps. The relaxation from 500 K to lower temperature is very slow.

The simulation by NAMD_k can explain most important experimental results. Different experimental groups reported that when $E_{\text{ini}} < 0.2$ eV, slow decay via acoustic phonons plays a role.[41–45] while when $E_{\text{ini}} > 0.2$ eV, the hot electrons can efficiently scatter with the optical phonons.[34, 38, 41, 45] The timescale is of the same magnitude as our results. Especially, the strong coupling with the A_1 and E_{2g} modes and the quantized energy-loss are in excellent agreement with the report by Na et al.[38]. Our work also agrees with the theoretical study by Bernardi and co-workers based on the quasi-classical time-dependent Boltzmann transport equation (rt-BTE).[40] It can be noted that hot electron relaxation mainly excites A_1 , E_{2g} , LA and TA. All of these phonons are in-plane modes. The out-of-plane phonon modes are not

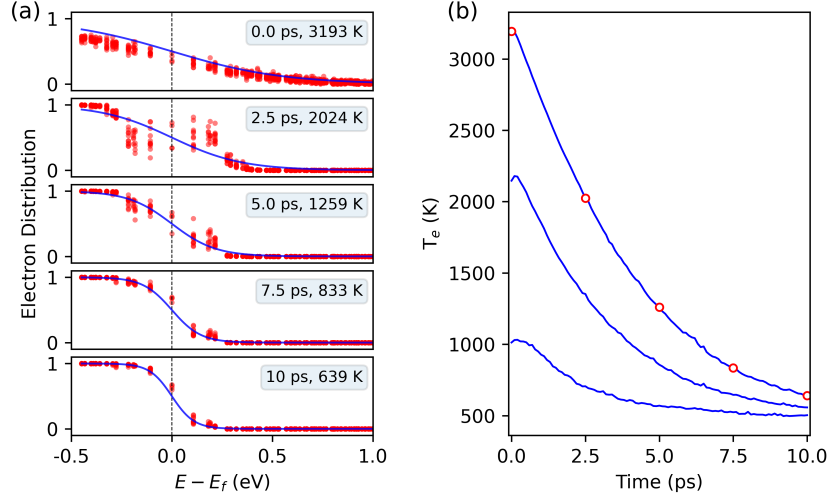


Fig. 4 (a) Snapshots of electron distribution at 0, 2.5, 5.0, 7.5 and 10 ps in multi-electron simulation with initial temperature of 3000 K. (b) Evolution of electron temperature for initial temperature of 1000, 2000 and 3000 K. The five panels in (a) correspond to the five small red circles in (b).

directly excited, and thus we propose the buckling of graphene requires a phonon-phonon interaction, which can be studied by the rt-BTE method.[40]

Comparing with NAMD_r, the NAMD_k method has a significant advantage treating solid state systems. First, only the *e-ph* coupling based on the calculation with the unit cell is required for NAMD_k. By contrast, for NAMD_r, the AIMD simulation and the electronic structure calculations for each time step along the AIMD trajectory using a supercell are required. The computational cost is significantly reduced by NAMD_k. Second, the $|\psi_{n\mathbf{k}}(\mathbf{r}; \mathbf{R}_0)\rangle$ basis sets used here can be understood as diabatic basis sets. Each electronic state has a clear notion of band index and momentum. We do not need to re-order the electronic states when they cross each other, thus the well-known state crossing problem in surface hopping can be avoided.[46–50] Third, in the NAMD_k method, the *e-ph* coupling can be understood in the time domain. Especially, the time-dependent phonon excitation induced by electron relaxation can be achieved, which is helpful to understand the photo-induced lattice structure distortion, which can not be achieved by the NAMD_r method using CPA, where the lattice distortion is pre-determined by the AIMD simulation. [6, 15] It also provides a dynamical picture of the energy transport between the electron and the phonon subsystems at the *ab initio* level beyond the semi-classical two-temperature model.[51, 52] Finally, since the *e-ph* coupling considering the SOC effects, as well as the exciton-phonon coupling elements can be calculated based on previous studies,[19, 23] the NAMD_k method can be easily extended for the investigation of SOC promoted spin dynamics and exciton dynamics using GW + real-time Bethe-Salpeter equation (GW+rtBSE) framework. The major approximation used in the NAMD_k method is the harmonic approximation. It will be very important and interesting to consider anharmonic effects in this approach in the future.

4 Summary

The newly developed NAMD-**k** approach breaks the bottleneck of NAMD application to carrier dynamics in momentum space. Based on the harmonic approximation, the *e-ph* coupling matrix can be used to calculate the coupling between electronic states with different momenta, and the phonon excitation dynamics can be simulated simultaneously. The NAMD-**k** approach is applied to study the hot carrier dynamics in graphene. It is found that the optical phonon mode defines an energy threshold which separates the hot electron carrier dynamics into fast and slow regions with lifetimes of ps and ns, respectively. We propose the NAMD-**k** approach to be an indispensable tool in exploring excited carrier dynamics in the momentum space, paving a new pathway to the theoretical design of devices and materials for optoelectronics, valleytronics and solar energy conversion.

Acknowledgments. J.Z. acknowledges the support of the National Natural Science Foundation of China (NSFC), grant nos. 12125408, 11974322. Q.Z. acknowledges the support of the National Natural Science Foundation of China (NSFC), grant nos. 12174363. O.V.P. acknowledges funding of the US National Science Foundation, grant no. CHE-2154367. YL.S. contributed to this work before March 2022. Calculations were performed Hefei Advanced Computing Center, and Supercomputing Center at USTC.

References

- [1] Tisdale, W.A., Williams, K.J., Timp, B.A., Norris, D.J., Aydil, E.S., Zhu, X.Y.: Hot-electron transfer from semiconductor nanocrystals. *Science* **328**(5985), 1543–1547 (2010). <https://doi.org/10.1126/science.1185509>
- [2] Rahul, Singh, P.K., Singh, R., Singh, V., Bhattacharya, B., Khan, Z.H.: New class of lead free perovskite material for low-cost solar cell application. *Materials Research Bulletin* **97**, 572–577 (2018). <https://doi.org/10.1016/j.materresbull.2017.09.054>
- [3] Akimov, A.V., Neukirch, A.J., Prezhdov, O.V.: Theoretical insights into photoinduced charge transfer and catalysis at oxide interfaces. *Chemical Reviews* **113**(6), 4496–4565 (2013). <https://doi.org/10.1021/cr3004899>
- [4] Wang, Q.H., Kalantar-Zadeh, K., Kis, A., Coleman, J.N., Strano, M.S.: Electronics and optoelectronics of two-dimensional transition metal dichalcogenides. *Nature Nanotechnology* **7**(11), 699–712 (2012). <https://doi.org/10.1038/nnano.2012.193>
- [5] Crespo-Otero, R., Barbatti, M.: Recent advances and perspectives on nonadiabatic mixed quantum-classical dynamics. *Chemical reviews* **118**(15), 7026–7068 (2018)

- [6] Zheng, Q., Chu, W., Zhao, C., Zhang, L., Guo, H., Wang, Y., Jiang, X., Zhao, J.: Ab initio nonadiabatic molecular dynamics investigations on the excited carriers in condensed matter systems. *WIREs Computational Molecular Science* **9**(6), 1411 (2019). <https://doi.org/10.1002/wcms.1411>
- [7] Smallwood, C.L., Kaindl, R.A., Lanzara, A.: Ultrafast angle-resolved photoemission spectroscopy of quantum materials. *EPL (Europhysics Letters)* **115**(2), 27001 (2016). <https://doi.org/10.1209/0295-5075/115/27001>
- [8] Bovensiepen, U., Kirchmann, P.S.: Elementary relaxation processes investigated by femtosecond photoelectron spectroscopy of two-dimensional materials. *Laser & Photonics Reviews* **6**(5), 589–606 (2012). <https://doi.org/10.1002/lpor.201000035>
- [9] Sobota, J.A., He, Y., Shen, Z.-X.: Angle-resolved photoemission studies of quantum materials. *Reviews of Modern Physics* **93**(2), 025006 (2021). <https://doi.org/10.1103/RevModPhys.93.025006>
- [10] Sawada, S.-I., Nitzan, A., Metiu, H.: Mean-trajectory approximation for charge- and energy-transfer processes at surfaces. *Physical Review B* **32**(2), 851–867 (1985). <https://doi.org/10.1103/PhysRevB.32.851>
- [11] Li, X., Tully, J.C., Schlegel, H.B., Frisch, M.J.: Ab initio ehrenfest dynamics. *The Journal of chemical physics* **123**(8), 084106 (2005)
- [12] Meng, S., Kaxiras, E.: Real-time, local basis-set implementation of time-dependent density functional theory for excited state dynamics simulations. *Journal of Chemical Physics* **129**(5) (2008). <https://doi.org/10.1063/1.2960628>
- [13] Kolesov, G., Granas, O., Hoyt, R., Vinichenko, D., Kaxiras, E.: Real-time td-dft with classical ion dynamics: Methodology and applications. *Journal of Chemical Theory and Computation* **12**(2), 466–476 (2016). <https://doi.org/10.1021/acs.jctc.5b00969>
- [14] Wang, Z., Li, S.-S., Wang, L.-W.: Efficient real-time time-dependent density functional theory method and its application to a collision of an ion with a 2d material. *Physical Review Letters* **114**(6), 063004 (2015). <https://doi.org/10.1103/PhysRevLett.114.063004>
- [15] Akimov, A.V., Prezhd, O.V.: The pyxaid program for non-adiabatic molecular dynamics in condensed matter systems. *J Chem Theory Comput* **9**(11), 4959–72 (2013). <https://doi.org/10.1021/ct400641n>
- [16] Tully, J.C.: Molecular dynamics with electronic transitions. *The Journal of Chemical Physics* **93**(2), 1061–1071 (1990)

- [17] Cui, G., Thiel, W.: Generalized trajectory surface-hopping method for internal conversion and intersystem crossing. *The Journal of Chemical Physics* **141**(12), 124101 (2014). <https://doi.org/10.1063/1.4894849>
- [18] Zhang, X., Li, Z., Lu, G.: First-principles determination of charge carrier mobility in disordered semiconducting polymers. *Physical Review B* **82**(20), 205210 (2010). <https://doi.org/10.1103/PhysRevB.82.205210>
- [19] Jiang, X., Zheng, Q., Lan, Z., Saidi, W.A., Ren, X., Zhao, J.: Real-time ewald -bse investigations on spin-valley exciton dynamics in monolayer transition metal dichalcogenide. *Science Advances* **7**(10), 3759 (2021). <https://doi.org/10.1126/sciadv.abf3759>
- [20] Liu, J., Zhang, X., Lu, G.: Excitonic effect drives ultrafast dynamics in van der waals heterostructures. *Nano Letters* **20**(6), 4631–4637 (2020). <https://doi.org/10.1021/acs.nanolett.0c01519>
- [21] Zheng, Q., Saidi, W.A., Xie, Y., Lan, Z., Prezhdov, O.V., Petek, H., Zhao, J.: Phonon-assisted ultrafast charge transfer at van der waals heterostructure interface. *Nano Lett* **17**(10), 6435–6442 (2017). <https://doi.org/10.1021/acs.nanolett.7b03429>
- [22] Li, W., Zhou, L., Prezhdov, O.V., Akimov, A.V.: Spin-orbit interactions greatly accelerate nonradiative dynamics in lead halide perovskites. *ACS Energy Letters* **3**(9), 2159–2166 (2018). <https://doi.org/10.1021/acsenergylett.8b01226>
- [23] Zheng, Z., Zheng, Q., Zhao, J.: Spin-orbit coupling induced demagnetization in ni: Ab initio nonadiabatic molecular dynamics perspective. *Physical Review B* **105**(8), 085142 (2022). <https://doi.org/10.1103/PhysRevB.105.085142>
- [24] Liu, X.-Y., Yang, J.-J., Chen, W.-K., Akimov, A.V., Fang, W.-H., Cui, G.: Spin-orbit coupling accelerates the photoinduced interfacial electron transfer in a fullerene-based perovskite heterojunction. *The Journal of Physical Chemistry Letters* **12**(4), 1131–1137 (2021). <https://doi.org/10.1021/acs.jpclett.0c03782>
- [25] Tian, Y., Zheng, Q., Zhao, J.: Tensile strain-controlled photogenerated carrier dynamics at the van der waals heterostructure interface. *The Journal of Physical Chemistry Letters* **11**(3), 586–590 (2020). <https://doi.org/10.1021/acs.jpclett.9b03534>
- [26] Zhao, C., Zheng, Q., Zhao, J.: Excited electron and spin dynamics in topological insulator: A perspective from ab initio non-adiabatic molecular dynamics. *Fundamental Research* **2**(4), 506–510 (2022). <https://doi.org/10.1016/j.fmre.2022.03.006>

- [27] Sohier, T., Calandra, M., Mauri, F.: Density functional perturbation theory for gated two-dimensional heterostructures: Theoretical developments and application to flexural phonons in graphene. *Physical Review B* **96**(7), 075448 (2017). <https://doi.org/10.1103/PhysRevB.96.075448>
- [28] Monserrat, B.: Electron–phonon coupling from finite differences. *Journal of Physics: Condensed Matter* **30**(8), 083001 (2018). <https://doi.org/10.1088/1361-648x/aaa737>
- [29] Ye, Z.-Q., Cao, B.-Y., Yao, W.-J., Feng, T., Ruan, X.: Spectral phonon thermal properties in graphene nanoribbons. *Carbon* **93**, 915–923 (2015). <https://doi.org/10.1016/j.carbon.2015.06.008>
- [30] Park, C.-H., Giustino, F., Cohen, M.L., Louie, S.G.: Velocity renormalization and carrier lifetime in graphene from the electron-phonon interaction. *Physical Review Letters* **99**(8), 086804 (2007). <https://doi.org/10.1103/PhysRevLett.99.086804>
- [31] Park, C.-H., Giustino, F., Cohen, M.L., Louie, S.G.: Electron-phonon interactions in graphene, bilayer graphene, and graphite. *Nano Letters* **8**(12), 4229–4233 (2008). <https://doi.org/10.1021/nl801884n>
- [32] Brida, D., Tomadin, A., Manzoni, C., Kim, Y.J., Lombardo, A., Milana, S., Nair, R.R., Novoselov, K.S., Ferrari, A.C., Cerullo, G., Polini, M.: Ultrafast collinear scattering and carrier multiplication in graphene. *Nature Communications* **4**(1), 1987 (2013). <https://doi.org/10.1038/ncomms2987>
- [33] Gierz, I., Petersen, J.C., Mitrano, M., Cacho, C., Turcu, I.C.E., Springate, E., Stöhr, A., Köhler, A., Starke, U., Cavalleri, A.: Snapshots of non-equilibrium dirac carrier distributions in graphene. *Nature Materials* **12**(12), 1119–1124 (2013). <https://doi.org/10.1038/nmat3757>
- [34] Johannsen, J.C., Ulstrup, S., Cilento, F., Crepaldi, A., Zacchigna, M., Cacho, C., Turcu, I.C.E., Springate, E., Fromm, F., Raidel, C., Seyller, T., Parmigiani, F., Grioni, M., Hofmann, P.: Direct view of hot carrier dynamics in graphene. *Physical Review Letters* **111**(2), 027403 (2013). <https://doi.org/10.1103/PhysRevLett.111.027403>
- [35] Gierz, I., Calegari, F., Aeschlimann, S., Chávez Cervantes, M., Cacho, C., Chapman, R.T., Springate, E., Link, S., Starke, U., Ast, C.R., Cavalleri, A.: Tracking primary thermalization events in graphene with photoemission at extreme time scales. *Physical Review Letters* **115**(8), 086803 (2015). <https://doi.org/10.1103/PhysRevLett.115.086803>
- [36] Malic, E., Winzer, T., Wendler, F., Knorr, A.: Review on carrier multiplication in graphene. *physica status solidi (b)* **253**(12), 2303–2310

(2016)

- [37] Baudisch, M., Marini, A., Cox, J.D., Zhu, T., Silva, F., Teichmann, S., Massicotte, M., Koppens, F., Levitov, L.S., García de Abajo, F.J., Biegert, J.: Ultrafast nonlinear optical response of dirac fermions in graphene. *Nature Communications* **9**(1), 1018 (2018). <https://doi.org/10.1038/s41467-018-03413-7>
- [38] Na, M.X., Mills, A.K., Boschini, F., Michiardi, M., Nosarzewski, B., Day, R.P., Razzoli, E., Sheyerman, A., Schneider, M., Levy, G., Zhdanovich, S., Devereaux, T.P., Kemper, A.F., Jones, D.J., Damascelli, A.: Direct determination of mode-projected electron-phonon coupling in the time domain. *Science* **366**(6470), 1231 (2019). <https://doi.org/10.1126/science.aaw1662>
- [39] Caruso, F., Novko, D., Draxl, C.: Photoemission signatures of nonequilibrium carrier dynamics from first principles. *Physical Review B* **101**(3), 035128 (2020). <https://doi.org/10.1103/PhysRevB.101.035128>
- [40] Tong, X., Bernardi, M.: Toward precise simulations of the coupled ultrafast dynamics of electrons and atomic vibrations in materials. *Physical Review Research* **3**(2), 023072 (2021). <https://doi.org/10.1103/PhysRevResearch.3.023072>
- [41] Butscher, S., Milde, F., Hirtschulz, M., Malić, E., Knorr, A.: Hot electron relaxation and phonon dynamics in graphene. *Applied Physics Letters* **91**(20), 203103 (2007). <https://doi.org/10.1063/1.2809413>
- [42] Tse, W.-K., Das Sarma, S.: Energy relaxation of hot dirac fermions in graphene. *Physical Review B* **79**(23), 235406 (2009). <https://doi.org/10.1103/PhysRevB.79.235406>
- [43] Wang, H., Strait, J.H., George, P.A., Shivaraman, S., Shields, V.B., Chandrashekhar, M., Hwang, J., Rana, F., Spencer, M.G., Ruiz-Vargas, C.S., Park, J.: Ultrafast relaxation dynamics of hot optical phonons in graphene. *Applied Physics Letters* **96**(8), 081917 (2010). <https://doi.org/10.1063/1.3291615>
- [44] Strait, J.H., Wang, H., Shivaraman, S., Shields, V., Spencer, M., Rana, F.: Very slow cooling dynamics of photoexcited carriers in graphene observed by optical-pump terahertz-probe spectroscopy. *Nano Letters* **11**(11), 4902–4906 (2011). <https://doi.org/10.1021/nl202800h>
- [45] Zhang, H., Bao, C., Schüller, M., Zhou, S., Li, Q., Luo, L., Yao, W., Wang, Z., Devereaux, T.P., Zhou, S.: Self-energy dynamics and the mode-specific phonon threshold effect in kekulé-ordered graphene. *National Science Review* **9**(5), 175 (2022). <https://doi.org/10.1093/nsr/nwab175>

- [46] Chu, W., Prezhdo, O.V.: Concentric approximation for fast and accurate numerical evaluation of nonadiabatic coupling with projector augmented-wave pseudopotentials. *The Journal of Physical Chemistry Letters* **12**(12), 3082–3089 (2021). <https://doi.org/10.1021/acs.jpclett.0c03853>
- [47] Chu, W., Zheng, Q., Akimov, A.V., Zhao, J., Saidi, W.A., Prezhdo, O.V.: Accurate computation of nonadiabatic coupling with projector augmented-wave pseudopotentials. *The Journal of Physical Chemistry Letters* **11**(23), 10073–10080 (2020). <https://doi.org/10.1021/acs.jpclett.0c03080>
- [48] Fernandez-Alberti, S., Roitberg, A.E., Nelson, T., Tretiak, S.: Identification of unavoided crossings in nonadiabatic photoexcited dynamics involving multiple electronic states in polyatomic conjugated molecules. *The Journal of Chemical Physics* **137**(1), 014512 (2012). <https://doi.org/10.1063/1.4732536>
- [49] Qiu, J., Bai, X., Wang, L.: Crossing classified and corrected fewest switches surface hopping. *The Journal of Physical Chemistry Letters* **9**(15), 4319–4325 (2018). <https://doi.org/10.1021/acs.jpclett.8b01902>
- [50] Wang, L., Prezhdo, O.V.: A simple solution to the trivial crossing problem in surface hopping. *The Journal of Physical Chemistry Letters* **5**(4), 713–719 (2014). <https://doi.org/10.1021/jz500025c>
- [51] Wang, H., Strait, J.H., George, P.A., Shivaraman, S., Shields, V.B., Chandrashekhara, M., Hwang, J., Rana, F., Spencer, M.G., Ruiz-Vargas, C.S., Park, J.: Ultrafast relaxation dynamics of hot optical phonons in graphene. *Applied Physics Letters* **96**(8), 081917 (2010). <https://doi.org/10.1063/1.3291615>
- [52] Hale, P.J., Horne, S.M., Moger, J., Horsell, D.W., Hendry, E.: Hot phonon decay in supported and suspended exfoliated graphene. *Physical Review B* **83**(12), 121404 (2011). <https://doi.org/10.1103/PhysRevB.83.121404>

Supplemental Materials

for

Ab initio Real-Time Quantum Dynamics of Charge Carriers in Momentum Space

Zhenfa Zheng¹, Yongliang Shi^{1,2,3*}, Jin-jian Zhou⁴, Oleg V.
Prezhdo⁵, Qijing Zheng^{1*} and Jin Zhao^{1,6*}

^{1*} Department of Physics, ICQD/Hefei National Laboratory for
Physical Sciences at Microscale, and CAS Key Laboratory of
Strongly-Coupled Quantum Matter Physics, University of Science
and Technology of China, Hefei, 230026, Anhui, China .

^{2*} Center for Spintronics and Quantum Systemes, State Key
Laboratory for Mechanical Behavior of Materials, School of
Materials Science and Engineering, Xi'an Jiaotong University,
Xi'an, 710049, Shanxi, China .

^{3*} China 2 State Key Laboratory of Surface Physics and
Department of Physics, Fudan University, Shanghai, 200433,
China .

⁴ School of Physics, Beijing Institute of Technology, Beijing,
100081, China .

⁵ Departments of Chemistry, Physics, and Astronomy, University
of Southern California, Los Angeles, 90089, California, USA .

^{6*} Department of Physics and Astronomy, University of
Pittsburgh, Pittsburgh, 15260, Pennsylvania, USA .

*Corresponding author(s). E-mail(s): sylcliff@xjtu.edu.cn;
zqj@ustc.edu.cn; zhaojin@ustc.edu.cn;

1 Zero nonadiabatic coupling for Bloch states with different momenta

In the real-space *ab initio* nonadiabatic molecular dynamics (NAMD) approach (NAMD-**r**), the charge carrier dynamics is mainly determined by the nonadiabatic coupling (NAC), which can be written as:

$$\begin{aligned} d_{m\mathbf{k}',n\mathbf{k}} &= \langle \psi_{m\mathbf{k}'} | \frac{d}{dt} | \psi_{n\mathbf{k}} \rangle \\ &\approx \frac{\langle \psi_{m\mathbf{k}'}(t) | \psi_{n\mathbf{k}}(t + \Delta t) \rangle - \langle \psi_{m\mathbf{k}'}(t + \Delta t) | \psi_{n\mathbf{k}}(t) \rangle}{2\Delta t}. \end{aligned} \quad (\text{S1})$$

For periodic systems, Bloch's theorem states that electronic state takes the form of a Bloch wave, i.e.

$$\psi_{n\mathbf{k}}(\mathbf{r}) = N_p^{-1/2} e^{i\mathbf{k}\cdot\mathbf{r}} u_{n\mathbf{k}}(\mathbf{r}), \quad (\text{S2})$$

where \mathbf{r} is the position of the electron, N_p is the number of unit cells, and $u_{n\mathbf{k}}(\mathbf{r})$ is a cell-periodic function, which satisfies

$$u_{n\mathbf{k}}(\mathbf{r} + \mathbf{L}_p) = u_{n\mathbf{k}}(\mathbf{r}), \quad (\text{S3})$$

where \mathbf{L}_p is the lattice vector of the p -th unit cell. Note that the Bloch wave $\psi_{n\mathbf{k}}$ is normalized in the Born-von Kármán (BvK) supercell, while the periodic part $u_{n\mathbf{k}}(\mathbf{r})$ is normalized in the unit cell. The overlap or inner product of two Bloch waves at different times becomes

$$\begin{aligned} \langle \psi_{m\mathbf{k}'}(t') | \psi_{n\mathbf{k}}(t) \rangle &= N_p^{-1} \int e^{-i(\mathbf{k}'-\mathbf{k})\cdot\mathbf{r}} u_{m\mathbf{k}'}^*(\mathbf{r}) u_{n\mathbf{k}}(\mathbf{r}) d\mathbf{r} \\ &= N_p^{-1} \sum_p \int_{p\text{-cell}} e^{-i(\mathbf{k}'-\mathbf{k})\cdot(\mathbf{r}+\mathbf{L}_p)} u_{m\mathbf{k}'}^*(\mathbf{r} + \mathbf{L}_p) u_{n\mathbf{k}}(\mathbf{r} + \mathbf{L}_p) d\mathbf{r} \\ &= N_p^{-1} \sum_p e^{-i(\mathbf{k}'-\mathbf{k})\cdot\mathbf{L}_p} \int_{\text{uc}} e^{-i(\mathbf{k}'-\mathbf{k})\cdot\mathbf{r}} u_{m\mathbf{k}'}^*(\mathbf{r}) u_{n\mathbf{k}}(\mathbf{r}) d\mathbf{r} \\ &= \delta_{\mathbf{k},\mathbf{k}'} \int_{\text{uc}} e^{-i(\mathbf{k}'-\mathbf{k})\cdot\mathbf{r}} u_{m\mathbf{k}'}^*(\mathbf{r}; t') u_{n\mathbf{k}}(\mathbf{r}; t) d\mathbf{r}, \end{aligned} \quad (\text{S4})$$

where the subscripts “ p -cell” and “uc” indicate that the integral is carried out within the p -th unit cell and the first unit cell, respectively. From the third line to the last line, we have used

$$N_p^{-1} \sum_p e^{-i(\mathbf{k}'-\mathbf{k})\cdot\mathbf{L}_p} = \delta_{\mathbf{k},\mathbf{k}'}. \quad (\text{S5})$$

From Eq. (S4), one can see that the inner product of two Bloch states at different times is zero for $\mathbf{k}' \neq \mathbf{k}$, thus the relating NAC is also zero. Apparently,

this excludes the possibility of using a unit cell to perform NAMD calculations were one to include different Bloch states. To circumvent this problem, in the NAMD_r approach, by introducing a large enough supercell, one can effectively fold the electronic states of different momenta \mathbf{k} to the Brillouin Zone center (Γ -point). Moreover, a large supercell can also accommodate phonon modes of different wavevectors \mathbf{q} , which can compensate the momentum difference needed for the crystal momentum conservation, resulting in a non-zero overlap and hence a non-zero NAC between the states.

2 Solving the Time-dependent Kohn-Sham (TDKS) equation

For quantum dynamics of excited carrier, we solve the time-dependent Shrödinger equation (TDSE)

$$i\hbar \frac{\partial}{\partial t} |\Psi(\mathbf{r}; \mathbf{R}(t))\rangle = \hat{H}^{el}(\mathbf{r}; \mathbf{R}(t)) |\Psi(\mathbf{r}; \mathbf{R}(t))\rangle. \quad (\text{S6})$$

Here, both electronic Hamiltonian $\hat{H}^{el}(\mathbf{r}; \mathbf{R}(t))$ and electronic wavefunction $|\Psi(\mathbf{r}; \mathbf{R}(t))\rangle$ depend on time through nuclear trajectory $\mathbf{R}(t)$.

In the nonadiabatic molecular dynamics simulation (NAMD) approach in momentum space (NAMD_k), starting with the equilibrium atomic structure \mathbf{R}_0 , the electronic Hamiltonian can be separated into two parts

$$\hat{H}^{el}(\mathbf{r}; \mathbf{R}(t)) = \hat{H}^0(\mathbf{r}; \mathbf{R}_0) + \Delta\hat{H}(\mathbf{r}; \mathbf{R}(t)), \quad (\text{S7})$$

where the first part $\hat{H}^0(\mathbf{r}; \mathbf{R}_0)$ is the Hamiltonian at equilibrium positions \mathbf{R}_0 , which is time-independent. The second part $\Delta\hat{H}$ is the variation of Hamiltonian, which is induced by nuclear displacements $\Delta\mathbf{R}(t) = \mathbf{R}(t) - \mathbf{R}_0$. As the nuclear coordinates only appear in the potential term $V(\mathbf{r}; \mathbf{R})$ in the electronic Hamiltonian $\hat{H}^{el} = \hat{T} + \hat{V}$, therefore $\Delta\hat{H}$ can be also written as

$$\Delta\hat{H}(\mathbf{r}; \mathbf{R}(t)) = \Delta V(\mathbf{r}; \mathbf{R}(t)) = V(\mathbf{r}; \mathbf{R}(t)) - V(\mathbf{r}; \mathbf{R}_0). \quad (\text{S8})$$

Then, we expand the electronic wavefunction by the eigenstates of equilibrium structure Hamiltonian $\hat{H}^0(\mathbf{r}; \mathbf{R}_0)$

$$|\Psi(\mathbf{r}; \mathbf{R}(t))\rangle = \sum_{n\mathbf{k}} c_{n\mathbf{k}}(t) |\psi_{n\mathbf{k}}(\mathbf{r}; \mathbf{R}_0)\rangle, \quad (\text{S9})$$

where \mathbf{k} represents the crystal momentum and n is the band index. The basis set $\{|\psi_{n\mathbf{k}}(\mathbf{r}; \mathbf{R}_0)\rangle\}$ are calculated in the framework of Kohn-Sham (KS) density functional theory (DFT), and satisfy

$$\hat{H}^0(\mathbf{r}; \mathbf{R}_0) |\psi_{n\mathbf{k}}\rangle = \epsilon_{n\mathbf{k}} |\psi_{n\mathbf{k}}\rangle, \quad (\text{S10})$$

where $\epsilon_{n\mathbf{k}}$ is eigen-energy of KS state $|\psi_{n\mathbf{k}}\rangle$. Here, it should be emphasized that the basis wavefunctions $\{|\psi_{n\mathbf{k}}\rangle\}$ are *time-independent* while the expanding coefficients $c_{n\mathbf{k}}(t)$ are *time-dependent*.

By substituting Eq. (S7)-(S10) into Eq. (S6) and multiplying by $\langle\psi_{m\mathbf{k}}|$ on both sides of equation, we get the time-dependent equation for the expanding coefficient

$$i\hbar \frac{d}{dt} c_{m\mathbf{k}'}(t) = \sum_{n\mathbf{k}} \left(H_{m\mathbf{k}',n\mathbf{k}}^0 + H_{m\mathbf{k}',n\mathbf{k}}^{ep} \right) c_{n\mathbf{k}}(t), \quad (\text{S11})$$

where $H_{m\mathbf{k}',n\mathbf{k}}^0$ is the matrix element of \hat{H}^0 , which is apparently diagonal

$$H_{m\mathbf{k}',n\mathbf{k}}^0 = \langle\psi_{m\mathbf{k}}|\hat{H}^0|\psi_{n\mathbf{k}}\rangle = \epsilon_{n\mathbf{k}} \delta_{mn,\mathbf{k}'\mathbf{k}}, \quad (\text{S12})$$

and $H_{m\mathbf{k}',n\mathbf{k}}^{ep}$ is the electron-phonon (*e-ph*) coupling matrix element

$$H_{m\mathbf{k}',n\mathbf{k}}^{ep} = \langle\psi_{m\mathbf{k}}|\Delta V|\psi_{n\mathbf{k}}\rangle. \quad (\text{S13})$$

To calculate the *e-ph* term, we expand the potential energy $V(\mathbf{r}; \mathbf{R}(t))$ in terms of nuclear displacements $\Delta\mathbf{R}(t)$. The potential to first order in displacements is

$$V(\mathbf{r}; \mathbf{R}(t)) = V(\mathbf{r}; \mathbf{R}_0) + \sum_{p\kappa} \left. \frac{\partial V(\mathbf{r}; \mathbf{R})}{\partial \mathbf{R}_{p\kappa}} \right|_{\mathbf{R}=\mathbf{R}_0} \cdot \Delta\mathbf{R}_{p\kappa}(t). \quad (\text{S14})$$

where the position of the nucleus κ in the p -th unit cell is denoted as $\mathbf{R}_{p\kappa} = \mathbf{L}_p + \tau_\kappa$, and \mathbf{L}_p is the cell vector. In practice, it is convenient to decompose nuclear displacements $\Delta\mathbf{R}(t)$ into normal modes

$$\Delta\mathbf{R}_{p\kappa}(t) = \sqrt{\frac{M_0}{N_p M_\kappa}} \sum_{\mathbf{q}\nu} e^{i\mathbf{q}\cdot\mathbf{L}_p} \mathbf{e}_{\kappa\nu}(\mathbf{q}) Q_{\mathbf{q}\nu}(t), \quad (\text{S15})$$

where M_0 is an arbitrary reference mass introduced to ensure that both sides of the equation have the dimension of length. Typically, M_0 is chosen to be the proton mass. $\mathbf{e}_{\kappa\nu}(\mathbf{q})$ is the polarization of the vibration wave corresponding to the wave vector \mathbf{q} and mode ν . $Q_{\mathbf{q}\nu}(t)$ is the normal mode coordinate of the corresponding mode. According to Eq. (S8),

$$\Delta V(\mathbf{r}; \mathbf{R}(t)) = \sqrt{\frac{1}{N_p}} \sum_{\mathbf{q}\nu} \sum_{p\kappa} \sqrt{\frac{M_0}{M_\kappa}} e^{i\mathbf{q}\cdot\mathbf{L}_p} \left. \frac{\partial V(\mathbf{r}; \mathbf{R})}{\partial \mathbf{R}_{p\kappa}} \right|_{\mathbf{R}=\mathbf{R}_0} \cdot \mathbf{e}_{\kappa\nu}(\mathbf{q}) Q_{\mathbf{q}\nu}(t). \quad (\text{S16})$$

Here, by defining

$$\partial_{\mathbf{q}\kappa} v(\mathbf{r}; \mathbf{R}_0) = \sum_p e^{-i\mathbf{q}\cdot(\mathbf{r}-\mathbf{L}_p)} \left. \frac{\partial V(\mathbf{r}; \mathbf{R})}{\partial \mathbf{R}_{p\kappa}} \right|_{\mathbf{R}=\mathbf{R}_0}, \quad (\text{S17})$$

and

$$\Delta_{\mathbf{q}\nu}v(\mathbf{r}; \mathbf{R}_0) = \sum_{\kappa} (M_0/M_{\kappa})^{1/2} \partial_{\mathbf{q}\kappa} V(\mathbf{r}; \mathbf{R}_0) \cdot \mathbf{e}_{\kappa\nu}(\mathbf{q}) l_{\mathbf{q}\nu}, \quad (\text{S18})$$

where $l_{\mathbf{q}\nu}$ is the “zero-point” displacement amplitude:

$$l_{\mathbf{q}\nu} = \sqrt{\frac{\hbar}{2M_0\omega_{\mathbf{q}\nu}}} \quad (\text{S19})$$

One can show that $\partial_{\mathbf{q}\kappa}v(\mathbf{r}; \mathbf{R}_0)$ and $\Delta_{\mathbf{q}\nu}v(\mathbf{r}; \mathbf{R}_0)$ are lattice-periodic functions. Then, Eq. (S16) can be written as

$$\Delta V(\mathbf{r}; \mathbf{R}(t)) = N_p^{-1/2} \sum_{\mathbf{q}\nu} e^{i\mathbf{q}\cdot\mathbf{r}} \Delta_{\mathbf{q}\nu}v(\mathbf{r}; \mathbf{R}_0) Q_{\mathbf{q}\nu}(t) l_{\mathbf{q}\nu}^{-1}. \quad (\text{S20})$$

By combining Eq. (S13), (S20) and (S2), we have

$$\begin{aligned} H_{m\mathbf{k}',n\mathbf{k}}^{ep} &= N_p^{-1/2} \sum_{\mathbf{q}\nu} N_p^{-1} \langle u_{m\mathbf{k}'} | e^{-i(\mathbf{k}'-\mathbf{k}-\mathbf{q})\cdot\mathbf{r}} \Delta_{\mathbf{q}\nu}v(\mathbf{r}; \mathbf{R}_0) | u_{n\mathbf{k}} \rangle Q_{\mathbf{q}\nu}(t) l_{\mathbf{q}\nu}^{-1} \\ &= N_p^{-1/2} \sum_{\mathbf{q}\nu} \langle u_{m\mathbf{k}'} | \Delta_{\mathbf{q}\nu}v(\mathbf{r}; \mathbf{R}_0) | u_{n\mathbf{k}} \rangle_{\text{uc}} \delta_{\mathbf{q},\mathbf{k}'-\mathbf{k}} Q_{\mathbf{q}\nu}(t) l_{\mathbf{q}\nu}^{-1} \\ &= N_p^{-1/2} \sum_{\nu} g_{mn\nu}(\mathbf{k}, \mathbf{q}) Q_{\mathbf{q}\nu}(t) l_{\mathbf{q}\nu}^{-1} \Big|_{\mathbf{q}=\mathbf{k}'-\mathbf{k}}, \end{aligned} \quad (\text{S21})$$

where the inner-product in the first line is an integral over the entire BvK supercell. Similar to the proof of Eq. (S4), one can show that the integral can be converted to an integral over the unit cell, provided that the momentum is conserved. $g_{mn\nu}(\mathbf{k}, \mathbf{q})$ is referred to as the *e-ph* matrix element

$$g_{mn\nu}(\mathbf{k}, \mathbf{q}) = \langle u_{m\mathbf{k}+\mathbf{q}} | \Delta_{\mathbf{q}\nu}v(\mathbf{r}; \mathbf{R}_0) | u_{n\mathbf{k}} \rangle_{\text{uc}}. \quad (\text{S22})$$

3 Surface Hopping

The fewest-switches surface hopping (FSSH) method represents time-evolving electron-nuclear system by an ensemble of trajectories, propagating under the influence of deterministic (via TDSE) and stochastic [via surface hopping(SH)] factors. Evolution of the system of interest is defined in a joint space combining classical phase-space for nuclei and discrete quantum states for electrons. The paths are constructed such that the FSSH probabilities for all states at all times, averaged over the trajectory ensemble, are equal to the corresponding probabilities obtained from the TDSE. The latter are given by diagonal

elements of the density matrix:

$$\rho_{m\mathbf{k}',n\mathbf{k}}(t) = c_{m\mathbf{k}'}^*(t)c_{n\mathbf{k}}(t). \quad (\text{S23})$$

The off-diagonal elements determine the probabilities of transitions between electronic states. For simplicity, we take the diagonal elements $\rho_{n\mathbf{k},n\mathbf{k}}$ as $\rho_{n\mathbf{k}}$ following. If the system is in state $n\mathbf{k}$ at time t , then the probability to leave this state at time $t + \Delta t$ is:

$$P_{n\mathbf{k}}(t; t + \Delta t) = \frac{\rho_{n\mathbf{k}}(t) - \rho_{n\mathbf{k}}(t + \Delta t)}{\rho_{n\mathbf{k}}(t)} = -\frac{\int_t^{t+\Delta t} \dot{\rho}_{n\mathbf{k}}(t) dt}{\rho_{n\mathbf{k}}(t)}. \quad (\text{S24})$$

From the definition of the density matrix, and from the TDSE, it follows that:

$$\dot{\rho}_{n\mathbf{k}}(t) = \sum_{m\mathbf{k}'} -\frac{2}{\hbar} \text{Im} \left(\rho_{m\mathbf{k}',n\mathbf{k}}^* H_{m\mathbf{k}',n\mathbf{k}}^{ep} \right). \quad (\text{S25})$$

Splitting the resulting hopping probability into various channels, $m\mathbf{k}'$, one obtains the probability of transition between the pair of states $n\mathbf{k} \rightarrow m\mathbf{k}'$:

$$P_{n\mathbf{k} \rightarrow m\mathbf{k}'}(t; t + \Delta t) = \frac{2}{\hbar} \frac{\int_t^{t+\Delta t} \text{Im} \left(\rho_{m\mathbf{k}',n\mathbf{k}}^* H_{m\mathbf{k}',n\mathbf{k}}^{ep} \right) dt}{\rho_{n\mathbf{k}}(t)}. \quad (\text{S26})$$

Note that each transition from $n\mathbf{k}$ to $m\mathbf{k}'$ corresponds to one e - ph scattering process, where the energy and crystal momentum must be conserved. However, Eq. (S26) can not guarantee the conservation law. To explicitly introduce the conservation law into the probability equation, recall that Fermi's golden rule gives the transition rate between two states

$$\frac{d}{dt} \mathcal{P}_{n\mathbf{k} \rightarrow m\mathbf{k}'}(t) = \frac{2\pi}{\hbar} |H_{m\mathbf{k}',n\mathbf{k}}^{ep}|^2 \times [\delta(\epsilon_{m\mathbf{k}'} - \epsilon_{n\mathbf{k}} - \hbar\omega_{\mathbf{q}\nu}) + \delta(\epsilon_{m\mathbf{k}'} - \epsilon_{n\mathbf{k}} + \hbar\omega_{\mathbf{q}\nu})]. \quad (\text{S27})$$

As a result, the modified hopping probability equation changes to

$$\tilde{P}_{n\mathbf{k} \rightarrow m\mathbf{k}'}(t; t + \Delta t) = \frac{2}{\hbar} \frac{\text{Im} \left(\rho_{m\mathbf{k}',n\mathbf{k}}^*(t) \tilde{H}_{m\mathbf{k}',n\mathbf{k}}^{ep} \right) \Delta t}{\rho_{n\mathbf{k}}(t)}, \quad (\text{S28})$$

where $\tilde{H}_{m\mathbf{k}',n\mathbf{k}}^{ep}$ is given by

$$\tilde{H}_{m\mathbf{k}',n\mathbf{k}}^{ep} = \frac{2\pi}{N_p} \sum_{\nu} |g_{mn\nu}(\mathbf{k}, \mathbf{q})|^2 (n_{\mathbf{q}\nu} + \frac{1}{2}) \times [\delta(\epsilon_{m\mathbf{k}'} - \epsilon_{n\mathbf{k}} - \hbar\omega_{\mathbf{q}\nu}) + \delta(\epsilon_{m\mathbf{k}'} - \epsilon_{n\mathbf{k}} + \hbar\omega_{\mathbf{q}\nu})]. \quad (\text{S29})$$

where the two δ function correspond to absorbing and emitting of phonon, respectively. In practical implementation, however, Gaussian function with certain broadening σ is used to approximate the Dirac δ -function

$$\delta(E) \approx \frac{1}{\sigma\sqrt{2\pi}} e^{-\frac{E^2}{2\sigma^2}}. \quad (\text{S30})$$

If the computed probability is negative, it is reset to zero. Thus, in general, the FSSH assigns a probability for transition from the current electronic state $n\mathbf{k}$ to the new state $m\mathbf{k}'$, as:

$$g_{n\mathbf{k} \rightarrow m\mathbf{k}'}(t; t + \Delta t) = \max \left[0, \tilde{P}_{n\mathbf{k} \rightarrow m\mathbf{k}'}(t; t + \Delta t) \right], \quad (\text{S31})$$

$$g_{n\mathbf{k} \rightarrow n\mathbf{k}}(t; t + \Delta t) = 1 - \sum_{m\mathbf{k}' \neq n\mathbf{k}} g_{n\mathbf{k} \rightarrow m\mathbf{k}'}(t; t + \Delta t). \quad (\text{S32})$$

In order to reflect the detailed balance condition, the hop rejection and velocity rescaling of the standard FSSH are replaced in the FSSH-CPA by scaling the transition probabilities $g_{n\mathbf{k} \rightarrow n\mathbf{k}}$ with the Boltzmann factor:

$$g_{n\mathbf{k} \rightarrow m\mathbf{k}'} \Rightarrow g_{n\mathbf{k} \rightarrow m\mathbf{k}'} b_{n\mathbf{k} \rightarrow m\mathbf{k}'}, \quad (\text{S33})$$

$$b_{n\mathbf{k} \rightarrow m\mathbf{k}'} = \begin{cases} \exp \left(-\frac{\epsilon_{m\mathbf{k}'} - \epsilon_{n\mathbf{k}}}{k_B T} \right) & \epsilon_{m\mathbf{k}'} > \epsilon_{n\mathbf{k}} \\ 1 & \epsilon_{m\mathbf{k}'} \leq \epsilon_{n\mathbf{k}} \end{cases}. \quad (\text{S34})$$

4 Test of k-grid Size and Energy Broadening

In graphene, the Dirac conical band structure results in a very small density of electronic states near the Fermi level (E_f), so a sufficiently dense \mathbf{k} -grid is required to accurately model the hot electron relaxation process. We have tested the simulation of hot electron relaxation with different \mathbf{k} -grid sizes, as shown in Fig. S1. It can be seen that with the increase of \mathbf{k} -point density, the electron relaxation process gradually converges. When the density of \mathbf{k} -points reaches $90 \times 90 \times 1$, the change of the hot electron relaxation process becomes negligible. However, it should be noted that as the electron energy gets closer to the Dirac point, the density of its electronic states decreases, so a denser \mathbf{k} -point is required. Hence, we use the \mathbf{k} -point grid of $150 \times 150 \times 1$ in simulations for $E_{\text{ini}} = 0.4 - 1.5 \text{ eV}$, and \mathbf{k} -point grid of $450 \times 450 \times 1$ in simulations for $E_{\text{ini}} < 0.3 \text{ eV}$.

In the e - ph coupling with energy conservation correct, to choose a reasonable energy broadening, we have tried different σ values to simulate the hot electron dynamics with initial energy of 1.0 eV ($E_{\text{ini}} = 1.0 \text{ eV}$). As shown in Fig. S2, the electron dynamics gets more and more elaborate as the energy broadening decreases 500 to 5 meV , while the relaxation time barely changes.

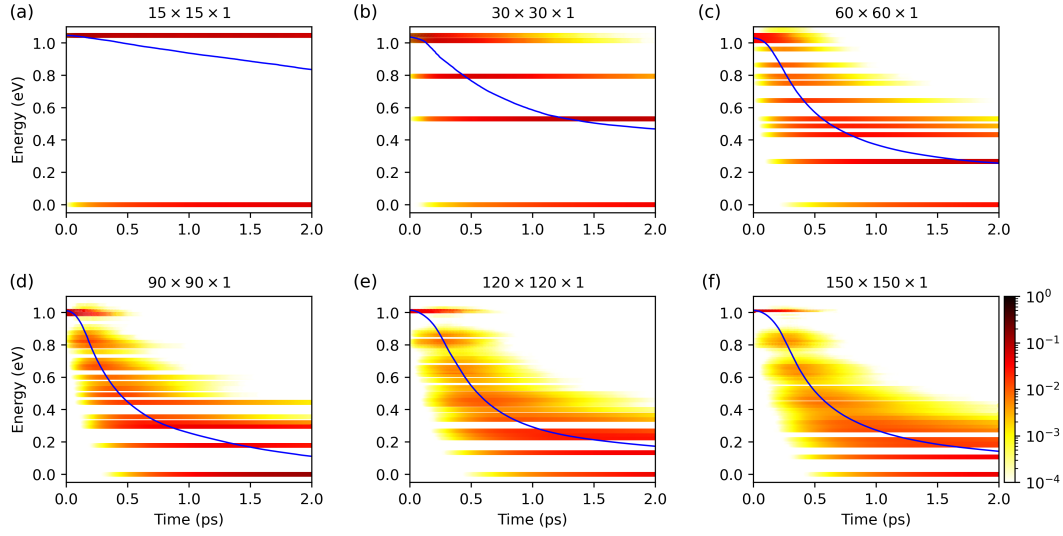


Fig. S1 Hot electron dynamics ($E_{ini} = 1.0 \text{ eV}$) with \mathbf{k} -points grid of (a) $15 \times 15 \times 1$, (b) $30 \times 30 \times 1$, (c) $60 \times 60 \times 1$, (d) $90 \times 90 \times 1$, (e) $120 \times 120 \times 1$, and (f) $150 \times 150 \times 1$. The color dots indicate the electron population in different states, and the blue line represents the averaged electron energy.

We can also find that the relaxation is blocked at low energy region for energy broadening is smaller than 10 meV. That is due to the finite \mathbf{k} -grid, which causes energy gap between different electronic states. To simulate the carrier relaxation in energy bands with continuous \mathbf{k} -grid, usually a smaller σ will provide more accurate results if the \mathbf{k} -grid sampling is dense enough. In this article we use $\sigma = 25 \text{ meV}$. To simulate the carrier dynamics across a band gap, the σ value can be estimated by the thermal oscillation of the electronic state at a certain temperature.

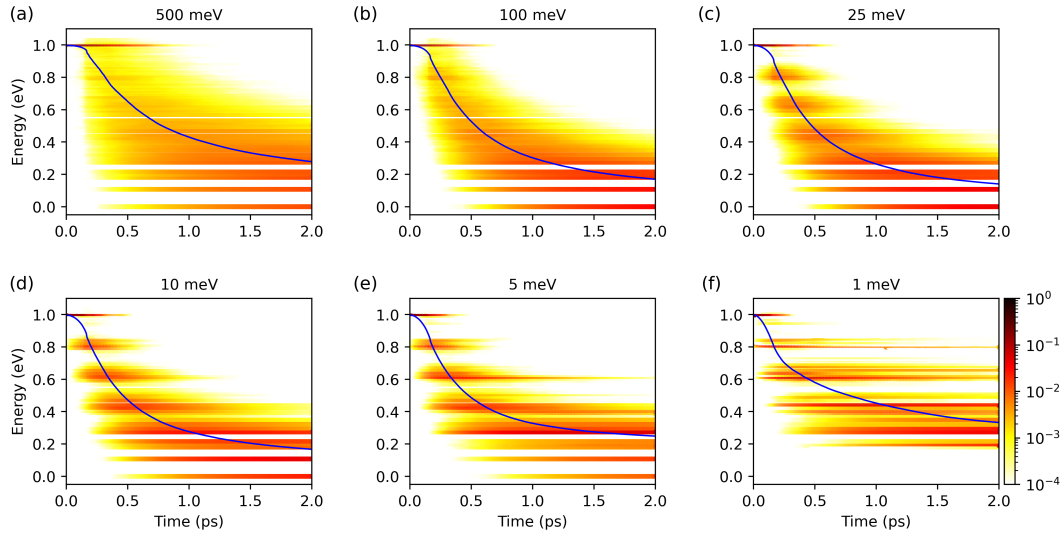


Fig. S2 Hot electron dynamics ($E_{ini} = 1.0 \text{ eV}$) with energy broadening of (a) 500 meV, (b) 100 meV, (c) 25 meV, (d) 10 meV, (e) 5 meV, and (f) 1 meV. The color dots indicate the electron population in different states, and the blue line represents the averaged electron energy.

5 Comparison with NAMD simulation in real space (NAMD_r)

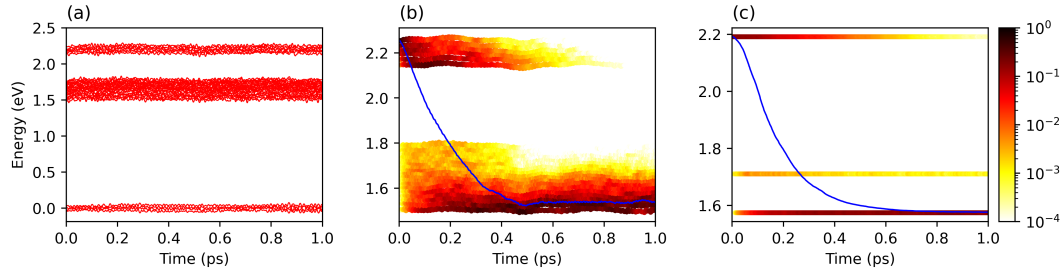


Fig. S3 (a) Energy evolution of KS states in the NAMD_r approach. The hot electron relaxation simulation from 2.2 eV to 1.6 eV using (b) NAMD_r method with $9 \times 9 \times 1$ supercell and (c) NAMD_k method with $9 \times 9 \times 1$ k -grid. The color dots indicate the electron population in different states, and the blue line represents the averaged electron energy.

In order to verify the validity of the NAMD_k method, we compare the calculation results of the NAMD_k with the NAMD_r approach. In the NAMD_r approach, a supercell is required to sample the phonon excitation with different \mathbf{q} points. Here we only simulate a $9 \times 9 \times 1$ supercell due to the limitation of computational cost. Then we compare the results with what NAMD_k obtains using $9 \times 9 \times 1$ k -grid. As the energy gaps are large for the $9 \times 9 \times 1$ supercell or k -grid close to the Fermi level, we choose to simulate the process of hot electron evolving from 2.2 eV to 1.6 eV, where the energy gaps are smaller relatively. As shown in Fig. S3, the states in NAMD_k simulation degenerate to 3 energy levels because we use the eigenstates of equilibrium structure Hamiltonian, and in fact the number of states equals to the NAMD_r simulation. Based on the NAMD_r simulation on graphene with $9 \times 9 \times 1$ supercell, we estimate the σ value to be 120 meV from the thermal oscillation. The results obtained by NAMD_r and NAMD_k agree with each other in substance. It clearly proves the validity of the NAMD_k approach.